AIAA JOURNAL
Vol. 40, No. 12, December 2002

Numerical Investigation of Transonic Resonance with a Convergent–Divergent Nozzle

Ching Y. Loh*
Taitech, Inc., Beavercreek, Ohio 45430
and
K. B. M. Q. Zaman†
NASA John H. Glenn Research Center at Lewis Field, Cleveland, Ohio 44135

At pressure ratios lower than the design value, convergent–divergent nozzles often undergo a flow resonance accompanied by the emission of acoustic tones. The phenomenon, driven by the unsteady shock within the divergent section of the nozzle, has been studied experimentally previously. The space–time conservation element solution element method is employed to numerically investigate the phenomenon. The computations are performed for a given nozzle geometry for several different pressure ratios. Sustained limit-cycle oscillations are encountered in all cases. The oscillation frequencies and their variation with pressure ratio, including a stage jump, agree well with the experimental results. The unsteady flow data confirm that stage 1 of the resonance (fundamental) involves a one-quarter standing wave, whereas stage 2 (third harmonic) involves a three-quarter standing wave within the divergent section of the nozzle. Details of the shock motion, the flow, and the near acoustic field are documented for one case each of stages 1 and 2.

I. Introduction

THIS paper is concerned with an aeroacoustic resonance often encountered with convergent–divergent nozzles when run near transonic conditions. The resonance is usually accompanied by the emission of intense acoustic tones. Whereas a casual observer may easily confuse it with the well-known screech tone, it has been shown to be different in character as well as origin. The frequency of the tone increases with increasing plenum pressure. The frequency variation may involve a staging behavior, that is, an abrupt jump in frequency. Whereas odd harmonic stages take place at lower pressures, the fundamental takes place over a wide range of higher pressures. Depending on nozzle geometry, the fundamental has been found to persist to pressure ratios as high as 5. The phenomenon has been identified and studied experimentally by Zaman et al.[1] For a discussion of background, technological relevance, and pertinent past work from the literature, see Ref. 1. A discussion of numerical works from the literature apparently capturing the same phenomenon, and the implication of those results, will be deferred to the discussion in Sec. V.

During the course of the experimental study a numerical study was initiated to complement the investigation. The space–time conservation-element and solution-element (CE/SE) method, to be elaborated shortly, was employed because of its past success with flows involving shocks and acoustic waves.[2] The calculations were first performed for a nozzle geometry and pressure ratio that corresponded to an experimental test condition. The result was encouraging in that the flow not only exhibited a quasi periodicity, but the frequency was also in agreement with the experimental result. Subsequent calculations at two other pressures captured the right trend in the frequency variation as well as the stage jump. These promising results prompted a further study. This was deemed well-justified not only to shed further light on the mechanism of the phenomenon but also to gain confidence in the computational fluid dynamics methodology.

The CE/SE method[3–5] was used as a numerical platform in the study. As demonstrated in previous papers, the CE/SE method is well suited for computing waves in compressible shear flows,[2] as well as vorticity/shock interactions,[6] both being pertinent in the phenomenon under consideration. Furthermore, based on the novel CE/SE nonreflecting boundary conditions (NRBC), it is expected that a small near-field computational domain would be sufficient and the simulation could be focused on the region of most importance in the resonance.

The objective of this paper is to describe the key results of the numerical study. The paper is arranged as follows. The axisymmetric CE/SE scheme is discussed in Sec. II. Initial and boundary conditions as well as the CE/SE NRBC are discussed in Sec. III. Numerical results are presented and compared with experimental results in Sec. IV, and further discussion and summary are given in Secs. V and VI.

II. Axisymmetric CE/SE Euler and Navier–Stokes Solvers

In this section, the CE/SE numerical scheme is summarized including 1) the Navier–Stokes CE/SE solver, 2) the structured triangulated grids used, and 3) the treatment of the source term and the two-dimensional axisymmetric approximation of large eddy simulation (LES) applied to the jet flow. The basic CE/SE principle and details of the Euler schemes can be found in the cited original papers.[3–5]

A. Conservation Form of the Unsteady Axisymmetric Navier–Stokes Equations

In general, the CE/SE method systematically solves a set of integral equations derived directly from the physical conservation laws and, hence, naturally captures shocks and other discontinuities in the flow. Both conservative flow variables and their derivatives are solved for simultaneously, and, consequently, the flow vorticity can be obtained without loss in accuracy. NRBCs are also easily implemented because of the flux-conservation formulation.

Consider a dimensionless conservation form of the unsteady axisymmetric Navier–Stokes equations of a perfect gas. Let ρ, u, v, p, and γ be the density, streamwise velocity component, radial velocity component, static pressure, and constant specific heat ratio, respectively. The axisymmetric Navier–Stokes equations then can be written in the following vector form:

Received 23 November 2001; revision received 30 May 2002; accepted for publication 3 June 2002.

*Research Scientist, 1430 Oak Court. Member AIAA.
†Aerospace Engineer, Turbomachinery and Propulsion Systems Division. Associate Fellow AIAA.

$$\boldsymbol{U}_t + \boldsymbol{F}_x + \boldsymbol{G}_y = \boldsymbol{Q} \tag{1}$$

where x, $y \geq 0$ and t are the streamwise and radial coordinates and time, respectively. The conservative flow variable vector $\boldsymbol{U}$ and the flux vectors in the streamwise and radial directions, $\boldsymbol{F}$ and $\boldsymbol{G}$, are given by

$$\boldsymbol{U} = \begin{pmatrix} U_1 \\ U_2 \\ U_3 \\ U_4 \end{pmatrix}, \qquad \boldsymbol{F} = \begin{pmatrix} F_1 \\ F_2 \\ F_3 \\ F_4 \end{pmatrix}, \qquad \boldsymbol{G} = \begin{pmatrix} G_1 \\ G_2 \\ G_3 \\ G_4 \end{pmatrix}$$

with

$$U_1 = \rho, \qquad U_2 = \rho u, \qquad U_3 = \rho v$$
$$U_4 = p/(\gamma - 1) + \rho(u^2 + v^2)/2$$

The flux vectors are further split into inviscid and viscous fluxes,

$$\boldsymbol{F} = \boldsymbol{F}_i - \boldsymbol{F}_v, \qquad \boldsymbol{G} = \boldsymbol{G}_i - \boldsymbol{G}_v$$

where the inviscid fluxes are the same as in the Euler equations,

$$F_{i1} = U_2, \qquad F_{i2} = (\gamma - 1)U_4 + \left[(3 - \gamma)U_2^2 - (\gamma - 1)U_3^2\right]/2U_1$$
$$F_{i3} = U_2U_3/U_1$$
$$F_{i4} = \gamma U_2U_4/U_1 - (\gamma - 1)U_2\left[U_2^2 + U_3^2\right]/2U_1^2$$
$$G_{i1} = U_3, \qquad G_{i2} = U_2U_3/U_1$$
$$G_{i3} = (\gamma - 1)U_4 + \left[(3 - \gamma)U_3^2 - (\gamma - 1)U_2^2\right]/2U_1$$
$$G_{i4} = \gamma U_3U_4/U_1 - (\gamma - 1)U_3\left[U_2^2 + U_3^2\right]/2U_1^2$$

and the viscous fluxes are

$$F_{v1} = 0, \qquad F_{v2} = \mu\left(2u_x - \frac{2}{3}\nabla \cdot \boldsymbol{V}\right)$$
$$F_{v3} = \mu(v_x + u_y)$$
$$F_{v4} = \mu\left[2uu_x + (u_y + v_x)v - \frac{2}{3}(\nabla \cdot \boldsymbol{V})u + \frac{\gamma}{Pr}\frac{\partial}{\partial y}\left(\frac{U_4}{U_1} - \frac{u^2 + v^2}{2}\right)\right]$$
$$G_{v1} = 0, \qquad G_{v2} = \mu(v_x + u_y)$$
$$G_{v3} = \mu\left(2v_y - \frac{2}{3}\nabla \cdot \boldsymbol{V}\right)$$
$$G_{v4} = \mu\left[2vv_y + (u_y + v_x)u - \frac{2}{3}(\nabla \cdot \boldsymbol{V})v + \frac{\gamma}{Pr}\frac{\partial}{\partial y}\left(\frac{U_4}{U_1} - \frac{u^2 + v^2}{2}\right)\right]$$

where u, v, u_x, u_y, v_x, and v_y are the x and y flow velocity components and their derivatives, respectively. They can be written in terms of the conservative variables U_1, U_2, U_3, and U_4. Pr is the Prandtl number and μ the viscosity. The velocity divergence is

$$\nabla \cdot \boldsymbol{V} = u_x + v_y + v/y$$

The right-hand source term $\boldsymbol{Q}$ is the same as in the axisymmetric Euler equations (see Ref. 7):

$$\boldsymbol{Q} = \begin{pmatrix} Q_1 \\ Q_2 \\ Q_3 \\ Q_4 \end{pmatrix}$$

where

$$Q_1 = -U_3/y, \qquad Q_2 = -U_2U_3/U_1y$$
$$Q_3 = -U_3^2/U_1y, \qquad Q_4 = -G_4/y$$

When (x, y, t) are considered as coordinates of a three-dimensional Euclidean space E_3 and Gauss's divergence theorem is used, it follows that Eq. (1) is equivalent to the following integral conservation law:

$$\oint_{S(V)} \boldsymbol{H}_m \cdot \mathrm{d}\boldsymbol{S} = \int_V Q_m \,\mathrm{d}V, \qquad m = 1, 2, 3, 4 \tag{2}$$

where $S(V)$ is the surface around a volume V in E_3 and $\boldsymbol{H}_m = (F_m, G_m, U_m)$.

B. Unstructured Grid for CE/SE

Even though in the present work structured triangulated grids are used, the CE/SE scheme is naturally adapted to unstructured triangular grids. The unstructured version of the CE/SE scheme can be briefly described using Fig. 1. Here, ΔABC is a typical triangular cell with its centroid (or center) at O, and D, E, F are the centroids (centers) of the neighboring triangular cells where the flow data at the previous time step are given. Each triangle center and its three neighboring triangle centers, when considered at two time levels, the previous and the present ones, form three cylindrical quadrilateral conservation elements (CEs), as shown in Fig. 1. In the space–time E_3 space, Eq. (2) is applied to the hexagon cylinder ADBECF (the volume V) that consists of these three quadrilateral CEs. The discrete finite volume approximation of Eq. (2) is then

$$\oint_{S(V)} \boldsymbol{H}_m^* \cdot \mathrm{d}\boldsymbol{S} = V(Q_m)_j^{n+1} \tag{3}$$

for $m = 1, 2, 3, 4$, where $\boldsymbol{H}_m^* = (F_m^*, G_m^*, U_m^*)$. The asterisk denotes that the quantity is a function or a variable in E_3 rather than a fixed value at certain node and time step. The right-hand side of Eq. (3), in general, is the volume V times the source term evaluated at an appropriate Gaussian quadrature node. Here, the Gaussian quadrature node is the center (or centroid) of the hexagon ADBECF at the new time level.

In the CE/SE scheme, the flux-conservation relation (2) in space–time is the only mechanism that transfers information between node points. A CE (here, quadrilateral cylinders) is the finite volume to which Eq. (2) is applied. Discontinuities are allowed to occur in the interior of a conservation element. A solution element (SE) associated with a grid node, for example, D, E, F in Fig. 1, is here a set of interface planes in E_3 that passes through this node, for example, DAA′D′, DBB′D′, EBB′E′, ECC′E′,etc.

At time level n, the solution variables $\boldsymbol{U}$, $\boldsymbol{U}_x$, and $\boldsymbol{U}_y$ are given at these three nodes D, E, and F. We are to solve $\boldsymbol{U}$, $\boldsymbol{U}_x$ and $\boldsymbol{U}_y$ at O′ at the new time level $n + 1$.

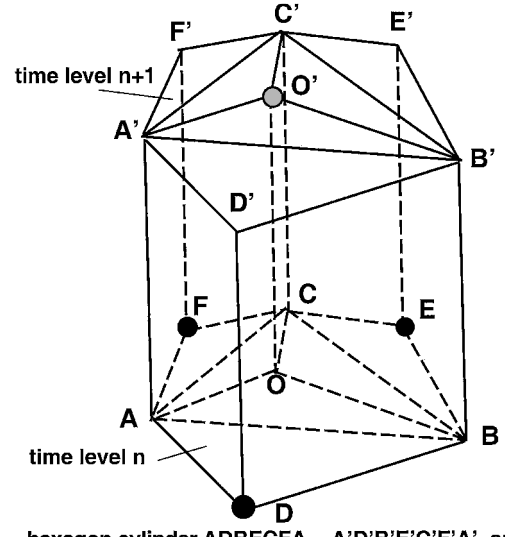

Fig. 1 CE/SE unstructured grid.

In principle, each of the three CEs provides four scalar equations when Eq. (2) is applied to it. In total, there are 12 scalar equations for the 12 scalar unknowns at O′. The problem is solvable. All of the unknowns are solved for based on these relations. No extrapolations (interpolations) across a stencil of cells are needed or allowed. However, in reality, $\boldsymbol{U}$ at the hexagon centroid at the new time level $n+1$ is first evaluated from Eq. (3). Consequently, $\boldsymbol{U}_x$ and $\boldsymbol{U}_y$ are solved with the necessary numerical dissipation added. Note that the hexagon centroid does not generally coincide with the centroid O′ of ΔABC. However, $\boldsymbol{U}$ at the triangle centroid O′ can be obtained by Taylor expansion. Details can be found in Ref. 5.

An important issue is how to calculate accurately the surface fluxes of the SEs. For this purpose, within a given SE (j, n), where j and n are the node index and time step, respectively, the flow variables are not only considered continuous but are also approximated by linear Taylor expansions:

$$\boldsymbol{U}^*(x, y, t; j, n) = \boldsymbol{U}_j^n + (\boldsymbol{U}_x)_j^n (x - x_j) + (\boldsymbol{U}_y)_j^n (y - y_j) + (\boldsymbol{U}_t)_j^n (t - t^n) \tag{4}$$

$$\boldsymbol{F}^*(x, y, t; j, n) = \boldsymbol{F}_j^n + (\boldsymbol{F}_x)_j^n (x - x_j) + (\boldsymbol{F}_y)_j^n (y - y_j) + (\boldsymbol{F}_t)_j^n (t - t^n) \tag{5}$$

$$\boldsymbol{G}^*(x, y, t; j, n) = \boldsymbol{G}_j^n + (\boldsymbol{G}_x)_j^n (x - x_j) + (\boldsymbol{G}_y)_j^n (y - y_j) + (\boldsymbol{G}_t)_j^n (t - t^n) \tag{6}$$

where j is the node index of D, E, or F. The partial derivatives of $\boldsymbol{F}$ and $\boldsymbol{G}$ can be related to the corresponding derivatives of $\boldsymbol{U}$ by using the chain rule, and $\boldsymbol{U}_t$ can be obtained from Eq. (1). Now, the surface flux can be calculated accurately by first evaluating the flux vectors at the geometrical center of the surface through the Taylor expansions (4–6). With unstructured grids, the CE/SE procedure is simplified and more adapted to complicated geometry. Also, the simple NRBCs described previously[2,6–8] still work well with an unstructured grid. The scheme is nominally second-order accurate in both space and time. More details about the unstructured CE/SE method can be found in Ref. 5. The weighted average a–ϵ CE/SE scheme with parameters $\alpha = 0$ and $\epsilon = 0.5$ is used here.

C. Treatment of the Source Term

The treatment is identical to the one used in Ref. 7 and is briefly reiterated here. Because the source term $\boldsymbol{Q} = \boldsymbol{Q}(\boldsymbol{U})$ itself is a function of the unknown $\boldsymbol{U}$ at the new time level, a local iterative procedure is needed to determine $\boldsymbol{U}$. The discretized integral equation (3) reduces to the form

$$\boldsymbol{U} - \boldsymbol{Q}(\boldsymbol{U})\Delta t = \boldsymbol{U}_H \tag{7}$$

where $\boldsymbol{U}_H$ is the local homogeneous solution, that is, the solution for $\boldsymbol{Q} = 0$ locally. Note that $\boldsymbol{U}_H$ only depends on the solution at the previous time step, that is, $\boldsymbol{U}_H$ is obtained using explicit formulas. A Newton iterative procedure to determine $\boldsymbol{U}$ is then

$$\boldsymbol{U}^{(i+1)} = \boldsymbol{U}^{(i)} - \left(\frac{\partial \Phi}{\partial \boldsymbol{U}}\right)^{-1} \left[\Phi\left(\boldsymbol{U}^{(i)}\right) - \boldsymbol{U}_H\right]$$

where i is the iteration number and

$$\Phi(\boldsymbol{U}) = \boldsymbol{U} - \boldsymbol{Q}(\boldsymbol{U})\Delta t$$

Normally, $\boldsymbol{U}$ at the previous time step is a good initial guess $\boldsymbol{U}^{(0)}$ and the procedure takes about two to three iterations to convergence.

D. LES

The CE/SE Navier–Stokes solver is applied to the interior of the convergent–divergent (C–D) nozzle. Outside the nozzle, however, to account for the strong momentum exchange in the jet shear layer, a simplified LES procedure similar to those used in Ref. 9 is adopted.

In this two-dimensional approximation of LES, a simple Smagorinsky's subgrid scale model is used for the eddy viscosity:

$$\mu_t = (C_s \Delta)^2 (2 S_{ij} S_{ij})^{\frac{1}{2}}$$

where

$$S_{ij} = \frac{1}{2}\left(\frac{\partial u_i}{\partial x_j} + \frac{\partial u_j}{\partial x_i}\right)$$

$\Delta = (\Delta x \Delta y)^{1/2}$, and $C_s = 0.1$. Then $\mu_t + \mu$ replaces μ in the Navier–Stokes CE/SE solver. As in Ref. 9, no LES averaging is used. The conservative variables $\boldsymbol{U}$ are spatially averaged already in the CE/SE finite volume procedure.

III. Computational Domain, Initial and Boundary Conditions

As stated earlier, an axisymmetric two-dimensional CE/SE Navier–Stokes solver was used. Note that high-Reynolds-number, inviscid calculations were first performed for the nozzle internal flow, that is, μ was set to zero for the viscous flux terms in the governing equations (Sec. II). With a uniform flow at the nozzle inlet and no-slip condition on the wall, the numerical process imposes a viscous effect, and there is a boundary-layer growth due to this numerical viscosity. Physical viscosity was later applied to simulate different Reynolds numbers, as discussed at the end of Sec. IV. The two-dimensional approximation of LES (Sec. II.D) was applied to the flow outside the nozzle to simulate the freejet properly. The calculation for the nozzle's internal flow should be deemed more relevant in the present study.

The computational domain started at the inlet of the convergent section of the nozzle as shown in Fig. 2. The domain extended over a rectangular subdomain outside the nozzle (62.2 cm in the axial direction x and 40.6 cm in the radial direction y; Fig. 3; in Fig. 2 the dimensions are shown in inches). The computation was started with the entire flow at rest and with the desired plenum pressure applied at the inlet boundary. A no-slip boundary condition was imposed on the nozzle wall. For the outer subdomain, ambient conditions were applied at the upstream inflow boundary, nonreflective conditions were applied at the upper and downstream boundaries, and a mirror-image reflective (symmetry axis) condition was applied at the bottom boundary.

The geometry of the nozzle can be seen in Fig. 2. The inlet diameter is 3.81 cm. The diameters at the nozzle's throat and exit are, respectively, $D_t = 0.76$ cm and $D_e = 1.02$ cm. The throat is located 5.08 cm downstream of the inlet. The convergent part follows a curved contour $y = f(x)$ as noted in Fig. 2, whereas the contour of

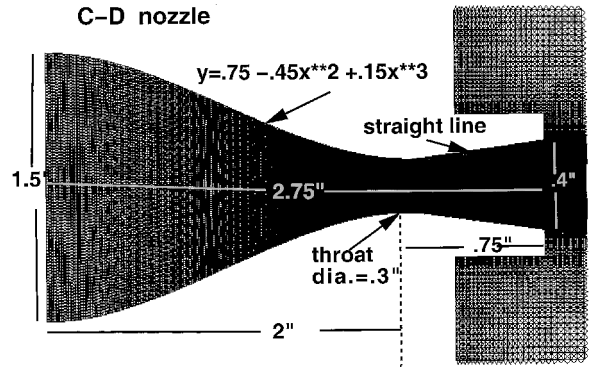

Fig. 2 Geometry of the C–D nozzle and unstructured grid.

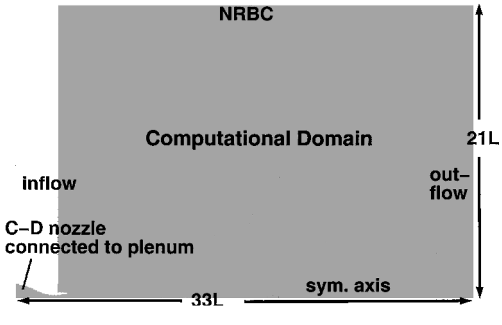

Fig. 3 Geometry of the entire computational domain.

the divergent part is a straight line. The geometry corresponds to case 3T2 described in Ref. 1.

In the experiments, it has been shown that the origin of the resonance is internal to the nozzle (unlike screech tones). Thus, the numerical investigation concentrates on the interior flow of the nozzle and the near field. Furthermore, the flow and the acoustic fields have been found to be of the axisymmetric mode in the experiments. Hence, the axisymmetric CE/SE code has been deemed sufficient, at least as a first attempt, in computing the flow. The ambient flow around the nozzle is assumed stationary.

The nozzle throat to exit length $L = 1.91$ cm is chosen as the length scale. The computational domain is a circular cylinder $33L$ long and $21L$ in radius. The triangulated grid is formed by cutting a rectangular cell into four triangles. These rectangular cells are nonuniform, and their numbers in the x and y directions are 200 and 225, respectively. In a typical case, the total number of triangles is 114,000. The last 10 cells in the streamwise direction have exponentially growing x size and serve as a buffer zone to ensure no numerical reflection from the outflow boundary. The grid resolution was deemed sufficient because a coarser grid produced the same results, as discussed shortly.

A. Initial Conditions

The pressure p_a and the speed of sound a_a in the ambient flow are used to scale the dependent variables. Initially, the flow of the entire domain is set at the ambient conditions, that is,

$$\rho_a = \gamma = 1.4, \qquad u_a = 0, \qquad v_a = 0, \qquad p_a = 1$$

$$\rho_i = \rho_a, \qquad u_i = u_a, \qquad v_i = v_a, \qquad p_i = p_a$$

Here, the subscripts a and i stand for ambient and initial, respectively.

Note that $p_a = 1$ corresponds to a dimensional pressure of 14.4 psi in the experiments. Consequently, the conservative flow variables and their spatial derivatives can be obtained in an easy way. Initially, all spatial derivatives are set to zero.

B. Boundary Conditions

At the domain inflow boundary outside the nozzle, the conservative flow variables and their spatial derivatives are specified to be the same as the ambient flow. The inlet of the C–D nozzle is connected to the plenum, which provides a constant pressure $p = p_0$ to drive the flow. The subscript 0 denotes the C–D nozzle inlet or the plenum. According to the experimental conditions, five different p_0 values (27.6, 55.2, 69.0, 103.5, and 138.0 kPa gauge) are chosen in the computation. The actual nondimensional p_0 values are 1.278, 1,556, 1.694, 2.042 and 2.389, respectively.

Following the experimental condition, the temperature in the plenum is assumed to be equal to that in the ambient. When the assumptions of constant total enthalpy and isentropic flow are used, it follows that the density ρ_0 at the nozzle inlet is related to the ambient pressure p_a and density ρ_a by

$$\rho_0 = (p_0/p_a)\rho_a$$

Flow at the nozzle inlet is at rest:

$$u_0 = v_0 = 0$$

No artificial forcing is imposed anywhere. As stated earlier, a no-slip condition is applied at the nozzle walls. At the symmetry axis, that is, $y = 0$, a reflective boundary condition is applied. At the top and outflow boundaries, the type 1 and type 2 CE/SE NRBCs as described in the next subsection are imposed, respectively.

C. NRBCs

In the CE/SE scheme, NRBCs are constructed to allow fluxes from the interior domain to a boundary CE smoothly exit to the exterior of the domain. There are several variants of the nonreflecting boundary condition, and in general, they have proven to be well suited for aeroacoustic problems.[2,6,7] The following are the ones employed in this paper.

For a grid node (j, n) lying at the outer radius of the domain, the NRBC (type 1) requires that

$$(\boldsymbol{U}_x)_j^n = (\boldsymbol{U}_y)_j^n = 0$$

while $\boldsymbol{U}_j^n$ is kept fixed at the initially given steady boundary value. At the downstream boundary, where there are substantial gradients in the radial direction, the NRBC (type 2) requires that

$$(\boldsymbol{U}_x)_j^n = 0$$

while $\boldsymbol{U}_j^n$ and $(\boldsymbol{U}_y)_j^n$ are now defined by simple extrapolation from the nearest interior node j', that is,

$$\boldsymbol{U}_j^n = \boldsymbol{U}_{j'}^{n-\frac{1}{2}}, \qquad (\boldsymbol{U}_y)_j^n = (\boldsymbol{U}_y)_{j'}^{n-\frac{1}{2}}$$

As will be observed later, these NRBCs are robust enough to allow a near-field computation without disturbing or distorting the flow and acoustic fields.

IV. Results

The calculations were carried out until a limit-cycle oscillation in the flowfield was reached. At this state, the flow property at a given point in the computational domain would undergo a quasi-periodic oscillation with varying time. The pressure oscillation at a given point in the computational domain for the $p_0 = 1.694$ case is shown in Fig. 4. The underlying periodicity in the time history should be apparent on an inspection. The power spectrum density corresponding to the data of Fig. 4, shown in Fig. 5, illustrates the periodicity unambiguously. The spectrum is clearly characterized by a peak at a frequency of about 2640 Hz. A large number of time steps (410,000–740,000) had to be run to achieve appropriate resolution on the low-frequency end of the spectrum, down to about 200 Hz. The bandwidth used in the spectral analysis is 40 Hz.

Also shown in Fig. 5 is the power spectrum density (PSD) calculated at approximately the same location using a coarser grid (80,000 cells). The amplitude of the peak is somewhat different from that for the fine grid. This is not unexpected because the phenomenon is not exactly periodic and the physical locations are not exactly the same. However, it is clear that the frequency of the dominant peak is the same. Thus, the fine grid resolution (114,000 cells) may be considered adequate.

The oscillation could be detected basically everywhere in the computational domain (although in regions corresponding to nodes the pressure oscillation might not be clear). The p spectrum obtained from data at a different point is shown in Fig. 6, as another example. Except for some difference in the spikes of higher frequencies, the overall spectrum and the dominant peak remains unchanged. Note that the data in Fig. 5 represent near-field acoustic pressure (outside the nozzle), whereas those in Fig. 6 represent pressure oscillation within the core of the flow. The flow oscillation frequencies are determined in a similar manner through spectral analysis for all five

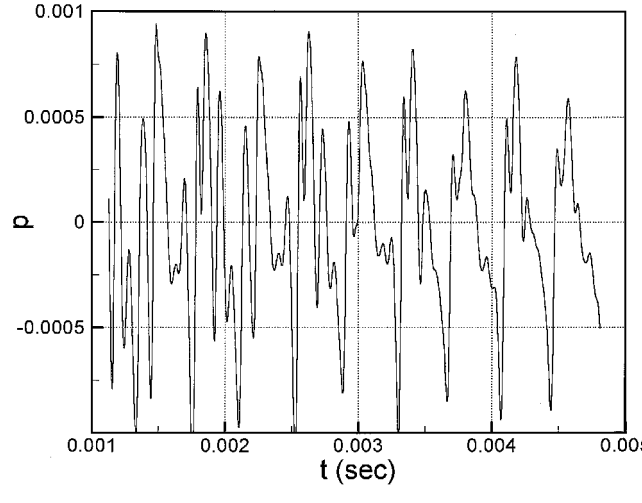

Fig. 4 Time history of pressure fluctuation at $x/L = 0.667$, $y/L = 2.66$.

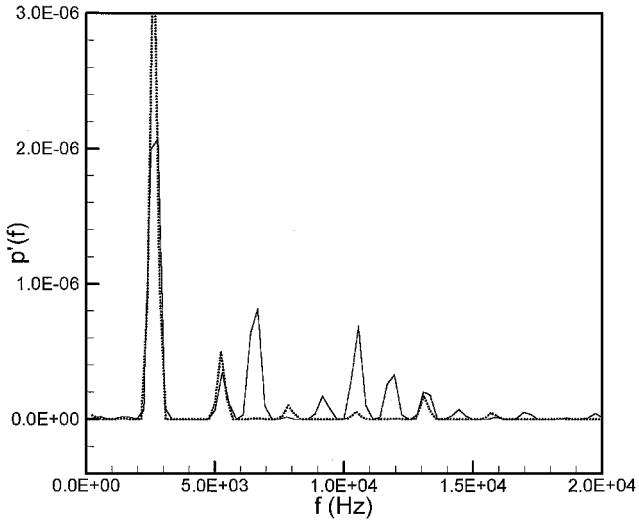

Fig. 5 PSD of fluctuating pressure at $x/L = 0.667, y/L = 2.66$: ——, fine grid (114,000 cells) and · · · ·, coarse grid (80,000 cells).

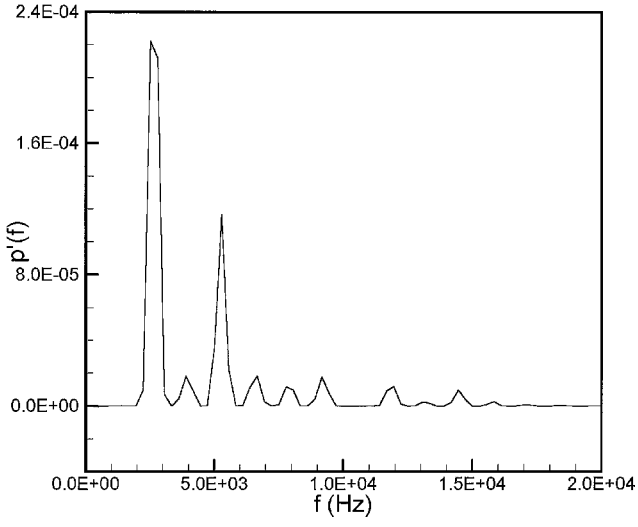

Fig. 6 PSD of fluctuating pressure within the convergent section at $x/L = -0.667, y/L = 0.20$.

operating pressures. These frequencies are compared with experimental data in Fig. 7.

Let us first briefly summarize the experimental results.[1] The frequency data were obtained by spectral analysis of a microphone signal. The data include screech tones as well as the transonic tones, as marked in Fig. 7. The latter phenomenon is the subject under consideration. Note that there is a staging behavior with the transonic tones. Two stages, marked in Fig. 7, are detected with the nozzle under consideration. From an analysis of data from a large number of nozzles, it was inferred that stage 1 represented the fundamental in the resonance, whereas stage 2 represented the next odd (third) harmonic. It was found that the presence of a shock within the upstream reaches of the divergent section was a necessary condition for the resonance to take place. A physical model for the underlying mechanism was proposed. In short, the unsteady shock was thought to act like a vibrating diaphragm, and resonance took place in a manner similar to that occurring in the simple (no-flow) acoustic resonance of a conical section with one end open and the other end closed. Thus, the fundamental was expected to involve a one-quarter (wavelength) standing wave within the diverging section, whereas the next (third) harmonic (stage 2) was expected to involve a three-quarter standing wave. Unsteady flow measurements did indicate the presence of such standing waves. However, the latter observation was not on firm ground because of the possibility of probe interference effects.

In Fig. 7, the numerical results for the resonant frequencies are shown by the solid circles. The results agree with the experimental

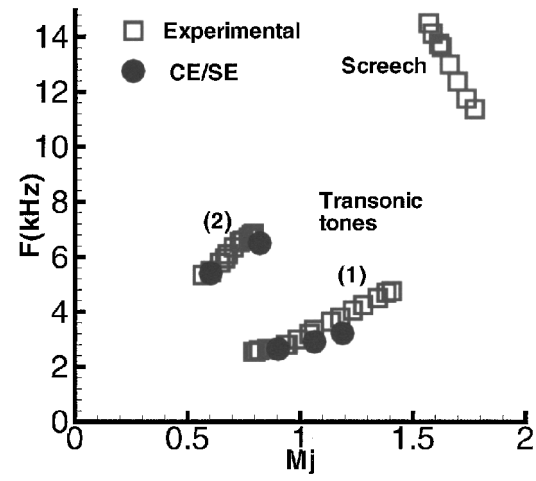

Fig. 7 Variation of tone frequency with M_j: □, experimental data for nozzle 3T2)[1] and ●, present numerical results.

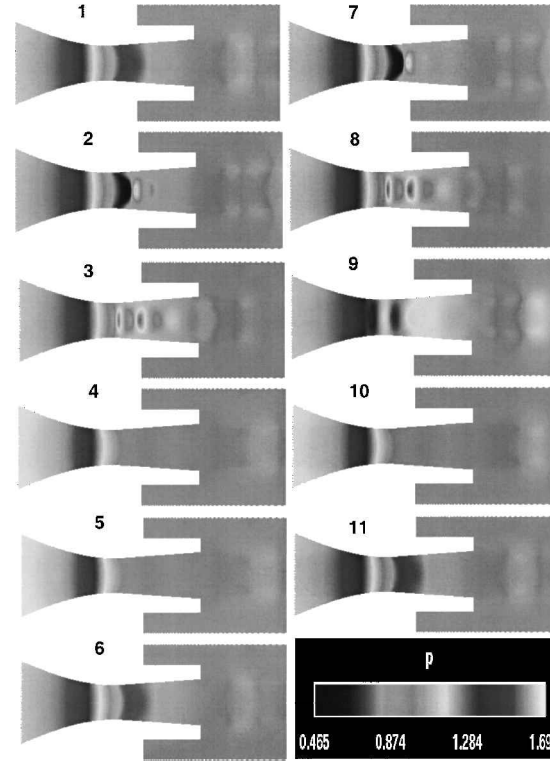

Fig. 8 Detailed flowfield pressure data for the fundamental case at $p_0 = 1.694$ (stage 1).

data very well. Not only are the trend of frequency variation within each stage and the stage jump, captured, but also the frequencies are predicted quite well.

Details of the flowfield were computed for two pressures, $p_0 = 1.278$ and 1.694, corresponding to stage 2 and stage 1 resonance, respectively. The static pressure distributions are shown in Fig. 8 for the fundamental case at $p_0 = 1.694$. The 11 frames span approximately $2T$, where T is the period of the oscillation. Thus, approximately on the sixth frame, the period is completed, and a similar distribution is expected as in the first frame. This is indeed the case, as can be seen. Numerical schlieren pictures, that is, distributions of $\partial\rho/\partial x$, corresponding to the instants of Fig. 8, are shown in Fig. 9. These illustrate the unsteady shock structure and its motion within the period. A shock (denoted by the sharp boundary between the lighter and darker regions) can be seen just past the throat of the nozzle. The shape and structure of the shock changes widely over the period. During part of the cycle, a clear bow-shaped front is seen (frames 1 and 6). During other parts of the cycle a lambda shock is

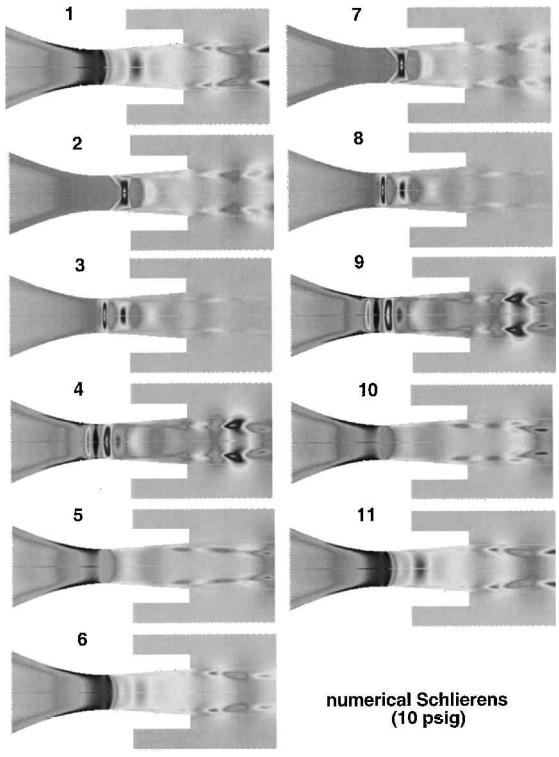

Fig. 9 Detailed numerical schlieren data for the fundamental case at $p_0 = 1.694$ (stage 1).

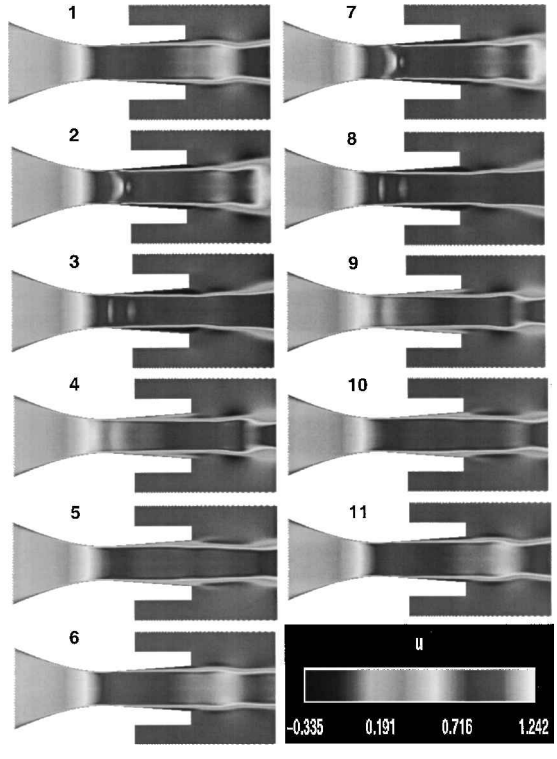

Fig. 10 Detailed flowfield axial velocity data for the fundamental case at $p_0 = 1.694$ (stage 1).

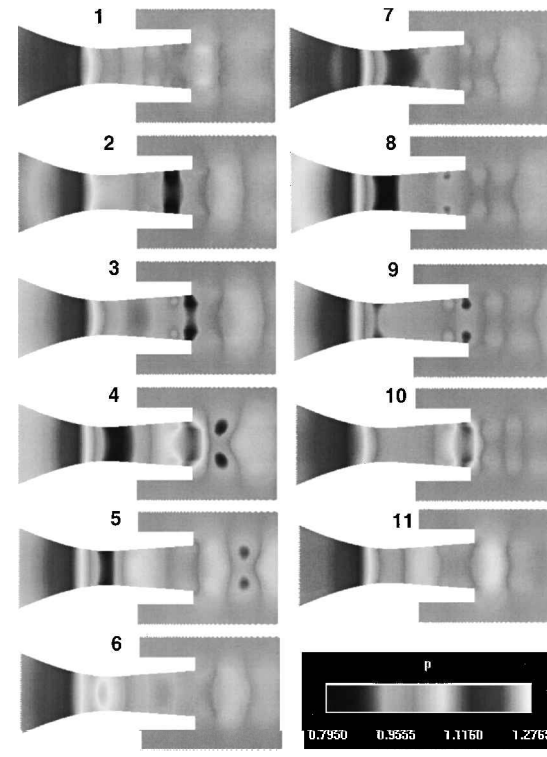

Fig. 11 Detailed flowfield pressure data for the case at $p_0 = 1.278$ (stage 2).

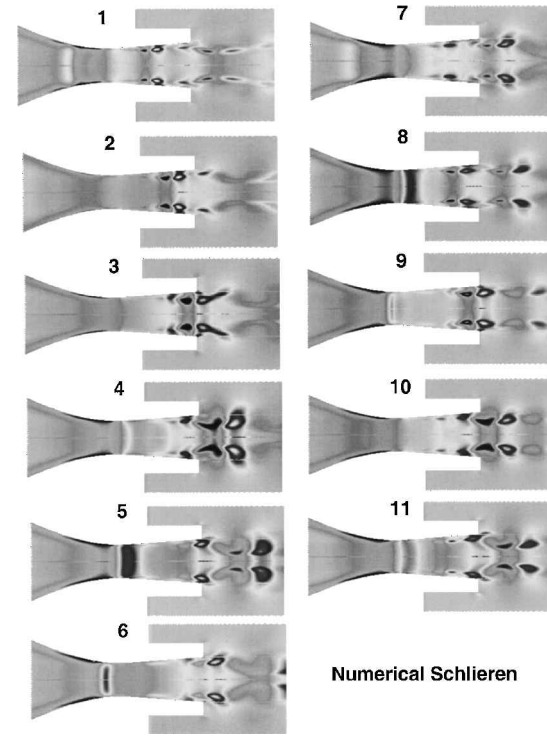

Fig. 12 Detailed numerical schlieren data for the case at $p_0 = 1.278$ (stage 2).

seen clearly (frames 2 and 7). Yet during other parts of the cycle, multiple fronts are noted. Corresponding distributions of the axial velocity U are shown in Fig. 10. A flow separation downstream of the throat of the nozzle can be observed. The length of the separated flow region changes over the period.

Flowfield details for the $p_0 = 1.278$ (stage 2) case are shown in Figs. 11–13, in a similar manner to those in Figs. 8–10. Here, an approximate repetition of the flow pattern every sixth frame can also be observed. However, it is not as clear as in the case of the fundamental. In any case, the completion of the period can be inferred, for example, by following the lighter patch of high-pressure region to the right of the nozzle exit in Fig. 11. It propagates downstream with increasing time step, until in the sixth frame a pattern similar to that in frame 1 reappears.

Refer back to the schlieren pictures for the $p_0 = 1.694$ case; a qualitatively similar shock motion may be noted in past experimental investigations. The schlieren pictures in Fig. 14 are from Hunter's experiment[10] of a two-dimensional C–D nozzle. (See Hunter[10]

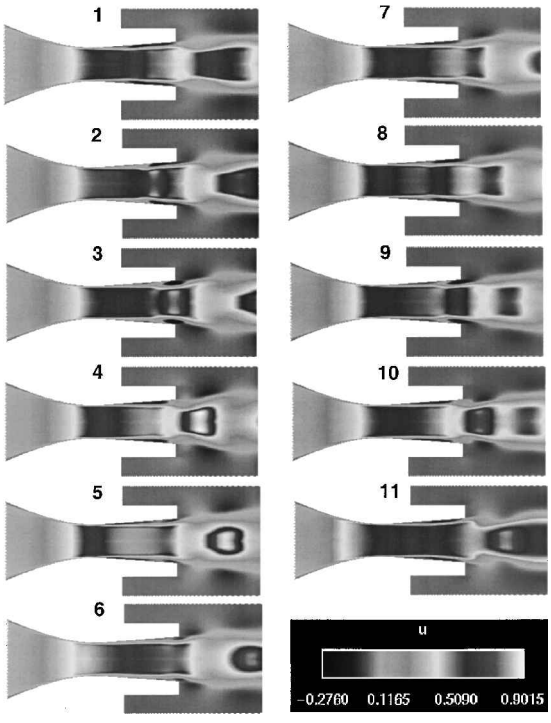

Fig. 13 Detailed flowfield axial velocity data for the case at $p_0 = 1.278$ (stage 2).

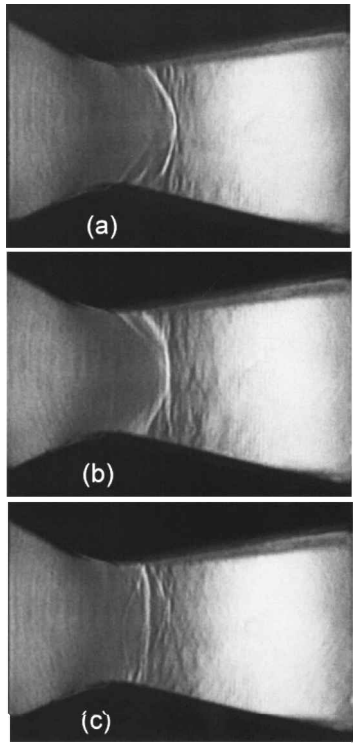

Fig. 14 Schlieren pictures of the internal shock structure for fundamental resonance at $M_j = 0.71$ for a rectangular nozzle, from Hunter's experiment.[10]

and Zaman et al.[1] for further details.) Compare, for example, the Figs. 14a, 14b and 14c with frames 1, 2, and 4 of Fig. 9.

The rms pressure fluctuation amplitudes were computed from the data on the centerline of the nozzle. The results are shown in Figs. 15a and 15b for the cases of the third harmonic (stage 2) and fundamental (stage 1), respectively. The throat is located at an abscissa value of 0, whereas the nozzle exit is at 1. In Fig. 15b, note that there is a pressure antinode somewhat downstream of the throat, whereas a node exists somewhat downstream of the exit. This

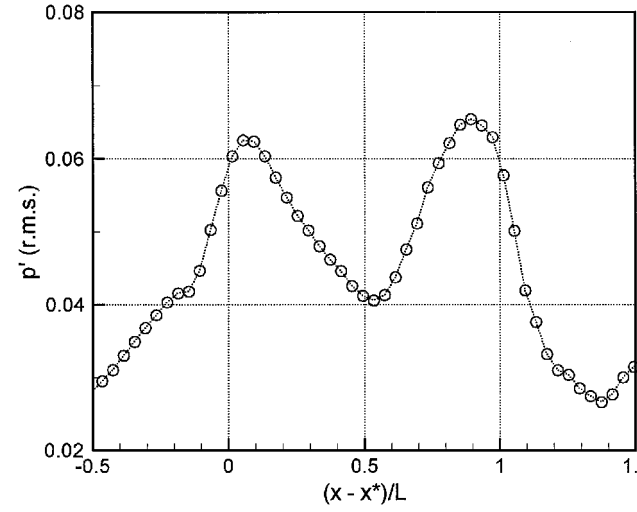

a)

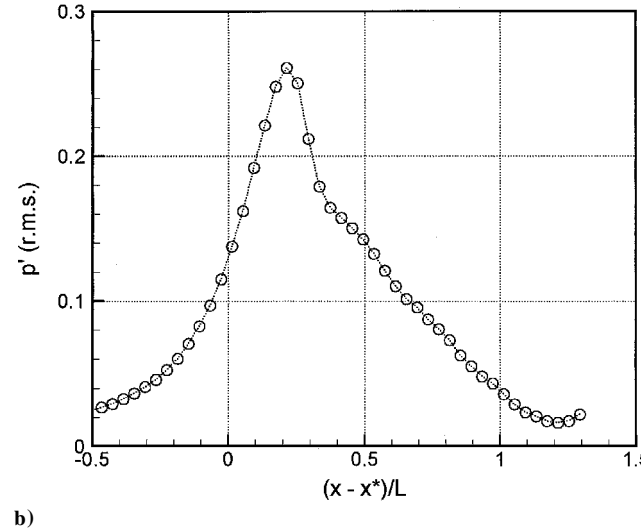

b)

Fig. 15 Time-averaged (rms) amplitude of fluctuating pressure along centerline of nozzle: a) $p_0 = 1.278$ case (stage 2) and b) $p_0 = 1.694$ case (stage 1).

clearly indicates the presence of a one-quarter standing wave within the divergent section. Similarly, a three-quarter standing wave is observed for stage 2 in Fig. 15a. The results of Fig. 15 agree with and confirm the presence of the standing waves that were conjectured from experimental evidence, as discussed earlier.

A recent experimental investigation in connection with flow metering using venturi nozzles (see Ref. 11) is worth mentioning. In Ref. 11, flow unsteadiness was observed at relatively low pressure ratios. Time-averaged data on recovery temperature clearly exhibited the presence of one-quarter, three-quarter, and even five-quarter standing waves within the divergent section.

In Fig. 16, the pressure amplitudes are shown for the fundamental case at a given instant. The acoustic radiation pattern at the resonance frequency is captured. The pattern is similar to that observed with duct acoustic resonance. For example, in Ref. 12, the pressure fluctuations for a resonating cylindrical duct were calculated. Whereas the internal pressure amplitudes apparently showed standing waves, the external radiation pattern appeared similar to that observed here.

Finally, the effect of Reynolds number on the resonance frequency is examined. In the experiments, the resonance tended to disappear with increasing pressure ratio (or M_j). Thus, the highest pressure ratio (2.042) was chosen for this Reynolds number sensitivity study. Computations were performed for three additional Reynolds numbers, calculated on the basis of ambient acoustic speed. The solid curve, representing high-Reynolds-number Re calculation was obtained in the same way as described earlier, that is, by setting μ

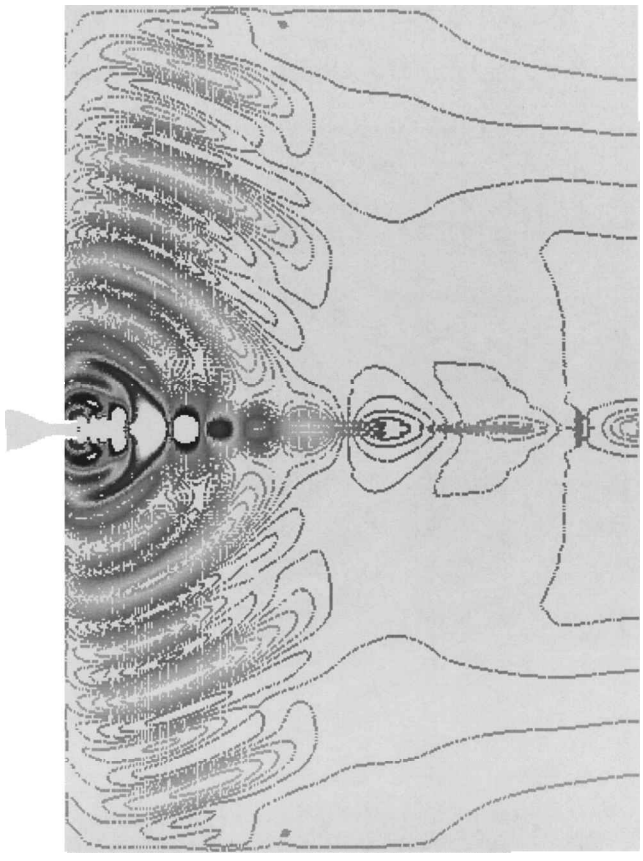

Fig. 16 Acoustic radiation for the fundamental case ($p_0 = 1.694$).

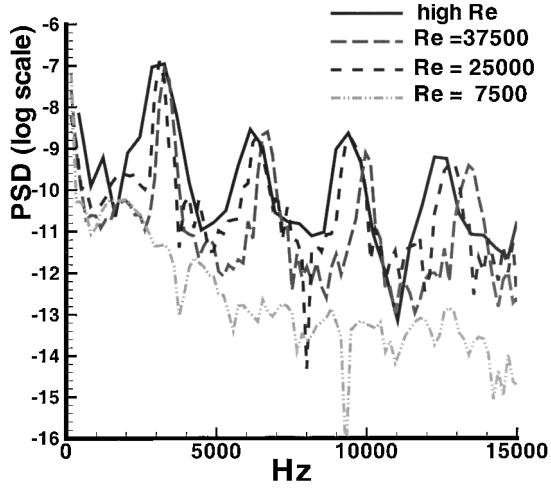

Fig. 17 PSD of fluctuating pressure at $x/L = 0.667, y/L = 2.667$, showing the influence of Reynolds number Re ($p_0 = 2.042$).

to zero (see Sec. III). This involved boundary layer with growth only due to numerical viscosity. The latter depends on grid size and other parameters of the computational procedure. An estimate of the numerical viscosity is not straightforward; however, the corresponding Reynolds number is thought to be quite high. The lower-Reynolds-number cases were obtained by setting correspondingly higher values of μ. Note that the nominal Reynolds number based on molecular viscosity is about 4.5×10^5.

The PSD of the fluctuating pressure is shown in Fig. 17. For brevity, these calculations were performed only for limited lengths of time so that the resolution in Fig. 17 is not as refined as in Figs. 5 and 6. The ordinate in Fig. 17 has a log scale and, thus, the higher harmonics appear prominently. It is clear that the resonance persists over a wide range of Reynolds numbers and the effect of high and moderate Reynolds number Re on the resonance frequency is quite small (about 2% at maximum). Only at the lowest Reynolds number Re does the oscillation disappear. Note that a decreasing Reynolds number Re is equivalent to a thickening of the boundary layer. The trend is, therefore, consistent with experimental observation that the resonance is suppressed on tripping of the boundary layer. However, the exact mechanism of the tripping effect remains unclear,[1] and further study, including computational work, is needed to obtain a full understanding.

V. Discussion

It is important to discuss certain past work that addressed the same or similar unsteady phenomenon. In the work reported in Ref. 13, a simulation of the experiments of Ref. 14 was performed. The experiment[14] reported a periodic unsteady flow through a two-dimensional transonic diffuser. The floor of the diffuser was flat, the two side-walls were parallel, and the top wall was C–D. An examination of the frequency data from this experiment (full discussion in Ref. 1) led to the inference that the observed unsteadiness must be of same morphology as of the subject phenomenon. Of relevance here is that the numerical simulation of Ref. 13 appeared to have captured the flow unsteadiness quite well. A two-dimensional, compressible, Reynolds averaged Navier–Stokes solver was used together with a two-equation turbulence model. The computation was started with an initial state determined from quasi-one-dimensional analysis. After sufficient time steps the flow settled into an oscillatory pattern. The period of oscillation for some of the cases agreed well with the data of Ref. 14. However, it was found that the diffuser flowfield and the frequency were very sensitive to the location of the downstream boundary.

Another numerical work[15] brought to the authors' attention also merits a discussion. This work concerned flow metering using venturi nozzles. Numerical simulation was conducted for flows similar to that of Ref. 11, discussed in connection with Fig. 15. An axisymmetric, unsteady, compressible Navier–Stokes solver was used. For certain conditions, a quasi-periodic fluctuation was observed in the computed flowfield. From the data provided in Ref. 15, it was not possible to determine whether the frequencies followed the correlation equations of Ref. 1. However, the symptoms appeared similar, and the unsteadiness seemed likely to be of the same origin as the transonic resonance.

Thus, to the authors' knowledge, at least two past numerical works also likely captured the transonic resonance phenomenon. The apparent ability to capture the phenomenon by "any" unsteady code is surprising because experimentally it is known to be very sensitive to operating conditions, especially to perturbations in the upstream boundary layer (see discussion of Fig. 17). Except for the similarity that all three simulations (the present and Refs. 13 and 15) involved axisymmetric or two-dimensional codes, different algorithms and procedures were followed. The upstream boundary layer in the present simulation is laminar, and that in Ref. 13 was apparently turbulent. We note that many aspects of the phenomenon, for example, the effect of boundary-layer tripping, remain far from completely understood. Further numerical study has the promise of advancing the understanding, and this is planned for the future.

VI. Summary

The unstructured CE/SE Navier–Stokes/Euler solver is applied to the transonic resonance phenomenon. It is clear that the essence of the phenomenon is captured by the computation. The frequency of the resonance and its variation with pressure ratio, including a stage jump, are captured quite well. A significant contribution of the present study is the results clearly show the characteristic standing waves (Fig. 15). This confirms that the underlying mechanism is similar to that of acoustic (no-flow) resonance of a duct having one end open and the other closed. This was conjectured in the earlier experimental work,[1] but the standing waves could not be measured with confidence because of probe interference.

The success in capturing the characteristics of the phenomenon attests to the validity of the numerical scheme. Other advantages of the CE/SE scheme include the effortless implementation (no special treatment, grid refinement, etc.), the simple but effective NRBC, and its shock-capturing capability.

As stated in Sec. III, most of the results in this paper are obtained by inviscid calculations for the internal flow. It can be viewed as a Navier–Stokes solution at a high Reynolds number with under-resolved boundary layer; the computed flow involves a boundary layer due to numerical viscosity only. Boundary-layer separation following the shock can be observed in Figs. 10 and 13. However, one may not expect that the details of the separated flow and the separation bubble would be captured faithfully by such a procedure. On the other hand, users of the CE/SE method have demonstrated its capability to capture shock structure relatively faithfully. Thus, one may infer that the shock and its unsteadiness, possibly due to flow separation, are the primary ingredients of the transonic resonance phenomenon and that the exact details of the separated boundary layer are here relatively unimportant.

Acknowledgments

This work was supported by the Supersonic Propulsion Technology Program of NASA John H. Glenn Research Center at Lewis Field. The authors are grateful to Nicholas Geogiadas and the referees for carefully reviewing the manuscript and providing valuable comments.

References

[1]Zaman, K. B. M. Q., Dahl, M. D., Bencic, T. J., and Loh, C. Y., "Experimental Investigation of 'Transonic Resonance' with Convergent–Divergent Nozzles," *Journal of Fluid Mechanics*, Vol. 463, 2002, pp. 313–343.

[2]Loh, C. Y., Hultgren, L. S., and Chang S.-C., "Computing Waves in Compressible Flow Using the Space–Time Conservation Element Solution Element Method," *AIAA Journal*, Vol. 39, No. 5, 2001, pp. 794–801; also AIAA Paper 98-0369, 1998.

[3]Chang, S. C., "The Method of Space–Time Conservation Element and Solution Element—A New Approach for Solving the Navier–Stokes and Euler Equations," *Journal of Computational Physics*, Vol. 119, 1995, pp. 295–324.

[4]Chang, S.-C., Wang, X.-Y., and Chow, C.-Y., "The Space–Time Conservation Element and Solution Element Method—A New High Resolution and Genuinely Multidimensional Paradigm for Solving Conservation Laws," *Journal of Computational Physics*, Vol. 159, 1999, pp. 89–136.

[5]Wang, X.-Y., and Chang, S.-C., "A 2-D Non-splitting Unstructured Triangular Mesh Euler Solver Based on the Space-Time Conservation Element and Solution Element Method," *Computational Fluid Dynamics Journal*, Vol. 8, 1999, pp. 309–325.

[6]Loh, C. Y., Hultgren, L. S., Chang, S.-C., and Jorgenson, P. C. E., "Vortex Dynamics Simulation in Aeroacoustics by the Space-Time Conservation Element Solution Element Method," AIAA Paper 99-0359, Jan. 1999.

[7]Loh, C. Y., Hultgren, L. S., and Jorgenson, P. C. E., "Near Field Screech Noise Computation for an Underexpanded Supersonic Jet by the CE/SE Method," AIAA Paper 2001-2252, May 2001.

[8]Chang, S.-C., Himansu, A., Loh, C. Y., Wang, X. Y., Yu, S.-T., and Jorgenson, P. C. E., "Robust and Simple Non-Reflecting Boundary Conditions for the Space-Time Conservation Element and Solution Element Method," AIAA Paper 97-2077, July 1997.

[9]Bogey, C., Bailly, C., and Juvé, D., "Computation of the Sound Radiated by a 3-D Jet Using Large Eddy Simulation," AIAA Paper 2000-2009, June 2000.

[10]Hunter, C. A., "Experimental, Theoretical, and Computational Investigation of Separated Nozzle Flows," AIAA Paper 98-3107, July 1998.

[11]Ishibashi, M., and Takamoto, M., "Discharge Coefficients of Critical Nozzles with Step Near the Throat and Their Flow Field Estimated from Recovery Temperature Distribution," American Society of Mechanical Engineers, Fluids Engineering Div. Summer Meeting, ASME Paper FED-SM2001-18035, May 2001.

[12]Hu, F. Q., and Manthey, J. L., "Application of PML Absorbing Boundary Conditions to the Benchmark Problems of Computational Aeroacoustics," *Second CAA Workshop on Benchmark Problems*, edited by C. K. W. Tam and J. C. Hardin, NASA CP-3352, June 1997.

[13]Hsieh, T., and Coakley, T. J., "Downstream Boundary Effects on Frequency of Self-Excited Oscillations in Transonic Diffuser Flows," AIAA Paper 87-0161, Jan. 1987.

[14]Bogar, T. J., Sajben, M., and Kroutil, J. C., "Characteristic Frequencies of Transonic Diffuser Flow Oscillations," *AIAA Journal*, Vol. 21, No. 9, 1983, pp. 1232–1240.

[15]von Lavante, E., Zaichcial, A., Nath, B., and Dietrich, H., "Numerical and Experimental Investigation of Unsteady Effects in Critical Venturi Nozzles," *Flow Measurement and Instrumentation*, Vol. 11, 2000, pp. 257–264.

H. M. Atassi
Associate Editor